

Effect of Element Distortion on the Numerical Dispersion of Spectral Element Methods

S. P. Oliveira¹ and G. Seriani^{2,*}

¹ *Departamento de Matemática, Universidade Federal do Paraná, Curitiba-PR, 81531-980, Brazil.*

² *Istituto Nazionale di Oceanografia e di Geofisica Sperimentale, Borgo Grotta Gigante, 42/c, Sgonico (TS), 34010, Italy.*

Received 7 November 2009; Accepted (in revised version) 8 July 2010

Communicated by Jan S. Hesthaven

Available online 2 November 2010

Abstract. Spectral element methods are well established in the field of wave propagation, in particular because they inherit the flexibility of finite element methods and have low numerical dispersion error. The latter is experimentally acknowledged, but has been theoretically shown only in limited cases, such as Cartesian meshes. It is well known that a finite element mesh can contain distorted elements that generate numerical errors for very large distortions. In the present work, we study the effect of element distortion on the numerical dispersion error and determine the distortion range in which an accurate solution is obtained for a given error tolerance. We also discuss a double-grid calculation of the spectral element matrices that preserves accuracy in deformed geometries.

AMS subject classifications: 65C20, 65M60, 65M70, 65M15, 86A15, 65Z05

Key words: Spectral element method, dispersion analysis, slivering.

1 Introduction

Spectral element methods are high-order finite element methods that use collocation points derived from orthogonal polynomials with the goal of enhancing approximation properties, in the spirit of spectral methods [3]. Spectral elements have been used in fluid mechanics [12, 17, 26, 29] and wave propagation [5, 13, 16, 28, 36]. Both triangular (tetrahedral) and quadrilateral (hexahedral) elements have been developed with various collocation point schemes, which for quadrilateral (hexahedral) element may take the simple form of a cartesian product of either Gauss-Lobatto-Legendre (GLL, [4, 5, 12]) or Gauss-Lobatto-Chebyshev (GLC, [9, 18, 37, 39]) nodes.

*Corresponding author. *Email addresses:* saulopo@ufpr.br (S. P. Oliveira), gseriani@inogs.it (G. Seriani)

These methods are particularly popular in computational seismology because they are able to simulate long-wave propagation events with low numerical dispersion, when compared with finite difference or standard finite element methods. Quadrilateral (hexahedral in 3D) meshes are the standard choice in computational seismology [5] because they naturally inherit the best approximation properties from the optimality of the collocation points and the algorithmic structure from the 1D case. Mercerat et al. [23] applied recent triangular spectral element techniques to elastic wave propagation problems and noted that quadrangular elements are more efficient in these problems, although high-order methods with triangular and tetrahedral meshes have shown to be competitive in other fields [13]. However, mesh design is a major bottleneck in this field, and it is necessary to seek a trade-off between honouring geological features and keeping the deformation of the mesh elements small enough for the desired accuracy [5]. In fact, realistic complex geological model automatic mesh generators (e.g., [18, 27]) may produce millions of elements (or even more) that cannot be visually verified and some of them can be very distorted (slivers). Knowing in advance the maximum allowed error for a simulation, a maximum element distortion can then be imposed to the mesh generator for the desired accuracy.

The effect of mesh deformation on the accuracy of finite elements has long been recognized. Although optimal error estimates may be preserved, the constant present on the error estimate becomes progressively larger as the distortion increases [15]. Maday and Rønquist [20] analyzed GLL spectral elements on deformed geometries and find an estimate whose constant is greater than $|1/J|$, where J is the determinant of the Jacobian of the transformation. Note that J may be zero for cases where quadrilaterals collapse into triangles by coalescing two nodes [15].

Some of the known sources of error in distorted meshes are the ill conditioning generated when corner angles are nearly 180° [2] and the fact that the computation of stiffness matrices may lead to rational integrands [40]. While the former relies on mesh design, the latter can be controlled by numerical or analytical integration techniques (see current approaches to this issue in [40]).

Some authors have briefly addressed the accuracy of spectral elements on distorted meshes. Melenk et al. [22] advocated the need of over-integration to account for mesh distortion for Legendre spectral elements, while in [7, 20] this method was found to perform well with a standard set of integration points, even for large distortions.

One of the most significant measures of the accuracy of wave propagation modeling is numerical dispersion. Dispersion analysis is an essential tool for setting up discretization parameters for an efficient numerical simulation of wave propagation with a prescribed level of accuracy. The dispersion properties of low-order and high-order finite elements are well understood on Cartesian grids [1, 10, 32], but few authors have considered deformed grids [7, 38].

The purpose of this paper is to describe the dependency of accuracy on mesh distortion in a systematic manner, providing a better understanding of spectral element methods on complex geometries, as well as unresolved issues such as the need of over-

integration noted above. We measure accuracy by the phase velocity error and the mesh distortion by internal angles between element edges and by aspect ratio. The phase velocity error is studied with a new dispersion analysis methodology based on the Rayleigh quotient, which holds for any operator order and is easily extended from 1D to 2D and 3D [32, 34]. We present a new double-grid representation of the inverse Jacobian function to correctly compute GLC spectral element matrices without resorting to high-order quadratures or increasing the polynomial degree of the shape functions. This approach generalizes [17] and can be seen as a Taylor truncation of inverse Jacobians [40].

By assuming an unbounded, periodic mesh formed by the repetition of a patch of elements [7], we estimate the numerical phase velocity of spectral element approximations of the 2D acoustic wave equation. Such an estimate depends only on the local mass and stiffness matrices in the elements in the patch. Next, we compute these matrices using the methodologies from [17, 31]. Then, we discuss numerical experiments on several patterns of element deformation that reflect anomalies that may be present on automatically-generated meshes.

2 Dispersion analysis

We consider the 2D acoustic wave equation in an unbounded, homogeneous medium:

$$\ddot{u}(\mathbf{x}, t) = c^2 \Delta u(\mathbf{x}, t). \quad (2.1)$$

Let us write the spectral element semi-discretization in space of (2.1) in the form

$$\mathbf{M}\ddot{\mathbf{u}}^*(t) + c^2 \mathbf{K}\mathbf{u}^*(t) = \mathbf{0}, \quad (2.2)$$

where $\mathbf{u}^* = \{u_I^*(t)\}$ is the unknown solution vector with $u_I^*(t) \approx u(\mathbf{x}_I, t)$, where \mathbf{x}_I the I -th global mesh node, whereas \mathbf{M}, \mathbf{K} are the global mass and stiffness matrices, respectively. The superscript $*$ is employed to identify an object as a numerical approximation. Plugging into this system a harmonic plane wave $\mathbf{u}^*(t) = \exp(-i\omega^*t)\mathbf{w}$, where $\mathbf{w} = \{w_I\}$ and $w_I = \exp(i\boldsymbol{\kappa} \cdot \mathbf{x}_I)$, we find

$$\mathbf{K}\mathbf{w} = \chi^* \mathbf{M}\mathbf{w}, \quad \chi^* = \left(\frac{\omega^*}{c}\right)^2. \quad (2.3)$$

This is an over-constrained system of equations where the only unknown is χ^* . On the other hand, we may consider a weaker condition: that the residual $(\mathbf{K} - \chi^* \mathbf{M})\mathbf{w}$ be orthogonal to \mathbf{w} ; that is, $\overline{\mathbf{w}}^T (\mathbf{K} - \chi^* \mathbf{M})\mathbf{w} = 0$. From this Galerkin condition (see [14]) we find

$$\chi^* = \frac{\overline{\mathbf{w}}^T \mathbf{K}\mathbf{w}}{\overline{\mathbf{w}}^T \mathbf{M}\mathbf{w}}, \quad \text{i.e.,} \quad \omega^* = \omega^*(\boldsymbol{\kappa}) = c \sqrt{\frac{\overline{\mathbf{w}}^T \mathbf{K}\mathbf{w}}{\overline{\mathbf{w}}^T \mathbf{M}\mathbf{w}}}. \quad (2.4)$$

Note that χ^* is now well-defined and corresponds to the Rayleigh quotient associated with the generalized eigenvalue problem (2.3). The dispersion estimate (2.4) predicts the minimum number of grid points per wavelength (G) needed to keep the dispersion error

below a prescribed level α . For this purpose, we parametrize the wave vector κ with respect to G ; rewrite the approximate angular frequency ω^* as a function of G ; calculate the numerical phase (or group) velocity $c^* = c^*(G)$; and determine the lowest value \tilde{G} such that $|c^*(G) - c| \leq \alpha$ for any $G \geq \tilde{G}$ and for any direction of the wave vector κ .

We have shown in [33–35] that such a prediction agrees with the classical dispersion analysis and with the dispersion study proposed in [24]. Moreover, Eq. (2.4) gives a faster and computationally more efficient estimate for high order elements, since the evaluation of the Rayleigh quotient is simpler than computing eigenvalues. This is more evident on 2D and 3D analysis with distorted elements, where the eigenvalue problem cannot be reduced to 1D eigenvalue problems [7]. Further discussion on advantages and limitations of using Rayleigh quotients to analyze numerical dispersion may be found in [11, 35].

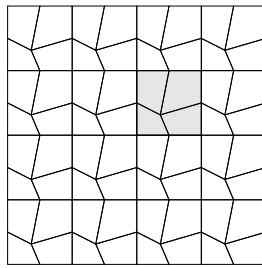


Figure 1: Mesh 4×16 elements generated by a patch of four non-rectangular elements ($N_e = 4$ and $n = 16$).

Let us consider a mesh that is formed by the repetition of a patch of N_e elements as in Fig. 1 and in [7]. An element-by-element evaluation of $\overline{w}^T K w$ yields

$$\overline{w}^T K w = \sum_{l=1}^n \left(\sum_{e=1}^{N_e} \overline{w}^{e,l,T} K^e w^{e,l} \right), \tag{2.5}$$

where K^e is the elemental stiffness matrix and $w^{e,l}$ is the restriction of the global array w to the e -th element $\Omega^{e,l}$ of the patch P_l ($1 \leq l \leq n$), which is given by

$$P_l = \bigcup_{e=1}^{N_e} \Omega^{e,l}. \tag{2.6}$$

Note that K^e does not depend on l . Moreover, if $x^{e,l}$ is the lower left vertex of P_l , then

$$w^{e,l} = \exp(i\kappa \cdot x^{e,l}) w^e, \tag{2.7}$$

where the vector w^e is defined by

$$w_j^e = \exp(i\kappa \cdot (x_j - x^{e,l})), \quad x_j \in \Omega^{e,l}.$$

Because the vector $x_j - x^{e,l}$ is invariant to P_l , we have that w^e does not depend on l . On the other hand, let us substitute (2.7) into (2.5):

$$\overline{w}^T K w = \sum_{l=1}^n \left(\sum_{e=1}^{N_e} \overline{\exp(i\kappa \cdot x^{e,l}) w^e}^T K^e \exp(i\kappa \cdot x^{e,l}) w^e \right) = n \sum_{e=1}^{N_e} \overline{w^e}^T K^e w^e. \tag{2.8}$$

Analogously, we find

$$\overline{w}^T M w = n \sum_{e=1}^{N_e} \overline{w}^e T M^e w^e, \quad (2.9)$$

where M^e is the elemental mass matrix. We have from (2.4), (2.5) and (2.9) that

$$\chi^* = \frac{\sum_{e=1}^{N_e} \overline{w}^e T K^e w^e}{\sum_{e=1}^{N_e} \overline{w}^e T M^e w^e}. \quad (2.10)$$

Note that χ^* does not depend on the number of patches n , hence it can be extended to an unbounded mesh, which is a standard assumption on dispersion analysis [1, 7]. Since Eq. (2.10) may be evaluated in any patch P_l , we drop the patch index l from here on; in particular, we refer to the element $\Omega^{e,l}$ of an arbitrary patch P_l as Ω^e .

For Cartesian meshes, expression (2.10) reduces to Rayleigh quotients of element matrices from 1D problems [32]. Similar estimates (2.10) hold in fully-discrete schemes (e.g., $\chi^* = (2\sin(\omega^* \Delta t/2)/\Delta t)^2$ in the case of time discretization by leapfrog scheme, see [25]).

3 Element matrices

To proceed with the analysis, we need to compute the terms in Eq. (2.10). Let us arrange the collocation points at an element Ω^e as $(N+1) \times (N+1)$ matrices (rather than $(N+1)^2$ vectors) and arrange nodal values likewise. For instance, $[w^e]$ is the $(N+1) \times (N+1)$ matrix associated with the vector w^e .

As described in the Appendix, if we choose Gauss-Lobatto-Legendre (GLL) collocation points and use these as integration points to compute the element mass and stiffness matrices, then

$$\overline{w}^e T M^e w^e = [W] : \left(\overline{[w^e]} \circ [w^e] \circ [J] \right), \quad (3.1a)$$

$$\overline{w}^e T K^e w^e = [W] : \left(\overline{[\nabla_1 w]} \circ [\nabla_1 w] \circ \frac{1}{[J]} + \overline{[\nabla_2 w]} \circ [\nabla_2 w] \circ \frac{1}{[J]} \right), \quad (3.1b)$$

where $[W]$ is the array that contains the GLL integration weights, $[\nabla_1 w]$ and $[\nabla_2 w]$ are nodal values of first-order derivatives of the interpolant of $[w^e]$, and $[J]$ are nodal values of the determinant of the Jacobian of the isoparametric transformation from $\hat{\Omega} = [-1, 1] \times [-1, 1]$ to Ω^e . The symbol \circ denotes the Haddamard product (A.14), whereas the colon denotes the double contraction operator defined in (A.17). Moreover, for the SEM with Gauss-Lobatto-Chebyshev (GLC) collocation points we find

$$\overline{w}^e T M^e w^e = \text{tr} \left(\overline{[w^e]}^T \cdot \mathbf{B}^+ \cdot [w^e] \right), \quad (3.2a)$$

$$\overline{w}^e T K^e w^e = \text{tr} \left(\overline{[\nabla_1 w]}^T \cdot \mathbf{B}^- \cdot [\nabla_1 w] + \overline{[\nabla_2 w]}^T \cdot \mathbf{B}^- \cdot [\nabla_2 w] \right), \quad (3.2b)$$

where

$$\mathbf{B}^+ = \mathbf{B}^T \cdot [\mathbf{J}] \cdot \mathbf{B} \quad \text{and} \quad \mathbf{B}^- = \mathbf{B}^T \cdot \left(\frac{1}{[\mathbf{J}]} \right) \cdot \mathbf{B},$$

and the elements of the matrix \mathbf{B} are expressed as

$$B_{l,p,q} = \int_{-1}^1 \phi_l(\zeta) \phi_p(\zeta) \phi_q(\zeta) d\zeta, \quad (3.3)$$

and $\phi_p(\zeta)$ are the 1D Lagrange interpolation shape functions of degree N defined by $\phi_p(\zeta_q) = \delta_{p,q}$, $\zeta_p = -\cos(\pi p/N)$, $0 \leq p, q \leq N$. The transposition operator and the dot product must be suited to third-order tensors, as in (A.23).

The computation of $\overline{\mathbf{w}^e}^T \mathbf{K}^e \mathbf{w}^e$ depends on an integral that involves the rational function $1/J$. To improve the accuracy of this computation in the case of GLC collocation points, we propose an approximation of the inverse Jacobian with an independent set of shape functions of higher degree:

$$\frac{1}{J}(\xi, \eta) = \sum_{q_1, q_2=0}^L \frac{1}{[[\mathbf{J}]]_{q_1, q_2}} \phi_{q_1}^L(\xi) \phi_{q_2}^L(\eta). \quad (3.4)$$

Here $\phi_p^L(\zeta)$ is the p -th 1D Lagrange interpolation shape function of degree L , $L \geq N$, whereas $[[\mathbf{J}]]$ is the $(L+1) \times (L+1)$ matrix that samples $J(\xi, \eta)$ at the collocation points of the temporary grid defined by $(\zeta_{q_1}^L, \zeta_{q_2}^L)$, $0 \leq q_1, q_2 \leq L$. The evaluation of Eq. (3.2) in this case is described in the Appendix.

This approach is based on the double-grid spectral element method [31], where the material properties are written with respect to shape functions of higher degree than the trial space. Although the original purpose of the double-grid method is to enhance resolution on heterogeneous media, it perfectly fits our aim of improving the resolution of $1/J$.

4 Numerical results

In this section we study the numerical dispersion under mesh distortion of the following spectral element methods (SEM):

GLC: consistent SEM with Gauss-Lobatto-Chebyshev (GLC) points [36];

GLL: mass-diagonal SEM with Gauss-Lobatto-Legendre (GLL) points [7].

The finite element meshes are generated as in Fig. 1 from the patches (a) to (d) in Fig. 2, and they represent various cases of element distortion. The chosen meshes do not represent real meshes, in general. The estimates lead to limit errors, and provide a constraint on the maximum element distortion that can be tolerated in real meshes.

We parametrize these meshes with the internal angle α indicated in the figure. As α approaches 180° , some elements degenerate and collapse into triangles or disappear.

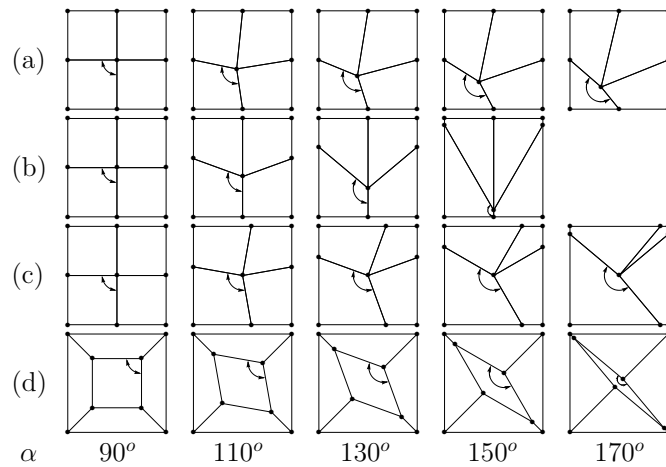


Figure 2: Summary of the element patches considered in the numerical experiments. The parameter α is the internal angle shown in each patch.

The dispersion error increases as the angle α increases, and we are able to obtain the maximum allowed element distortion for a given error tolerance.

Let $\kappa = \kappa(\cos\theta, \sin\theta)$. We evaluate κ from the number of grid points per wavelength

$$G = \frac{\lambda}{\Delta x} = \frac{2\pi}{|\kappa|\Delta x'} \tag{4.1}$$

where Δx is defined as the diagonal of any of the elements in the patches (a) to (c), or as the diagonal of the central element in the patch (d). We compute Δx when $\alpha = 90^\circ$ and use this value of Δx also in distorted elements.

The first experiment confirms that the sensitivity of the phase velocity error to mesh distortion decreases as the double-grid parameter L in (3.4) increases. This is illustrated in Fig. 3 with the fourth-degree GLC method. The choice $L = 12$ delivers sufficiently

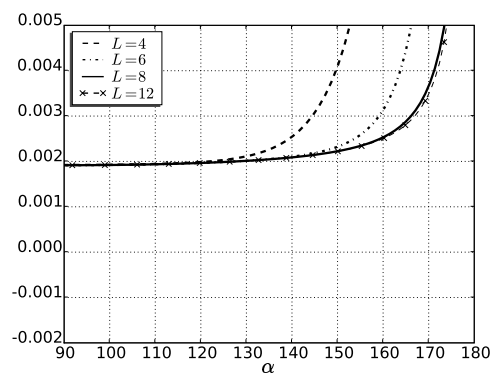


Figure 3: Average phase velocity error of the GLC method versus element distortion for the patch (d). We consider several degrees of resolution (L) of the inverse Jacobian function and take $N = 4$ and $G = 4$.

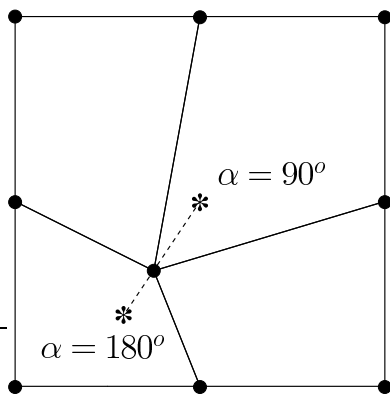


Figure 4: Location of the central node on element patch (a).

accurate results also for higher polynomial degrees and other mesh patterns, thus we will employ $L = 12$ in GLC from here on. We do not depart from the standard integration procedure for the GLL method in the experiments below.

The element patch (a) was employed by Cohen [7] to analyze the numerical dispersion of GLL spectral elements of degree up to five. Note that the central node of the patch moves along a direction that is not aligned with the diagonals or the sides of the patch (Fig. 4).

Let us first present a comparison with the work by Cohen in Fig. 5. Following the experiment on [7, pp. 232], we consider cubic elements and use nine grid points per wavelength. The relative difference between the phase velocity estimates from the eigenvalue that is closer to the acoustic mode and the Rayleigh quotient is of order 10^{-4} .

Fig. 6 shows the average phase velocity error $\varepsilon = (\omega^*/\kappa - c)/c$ as a function of the internal angle α when $G = 4$. We take the average error over the propagation directions

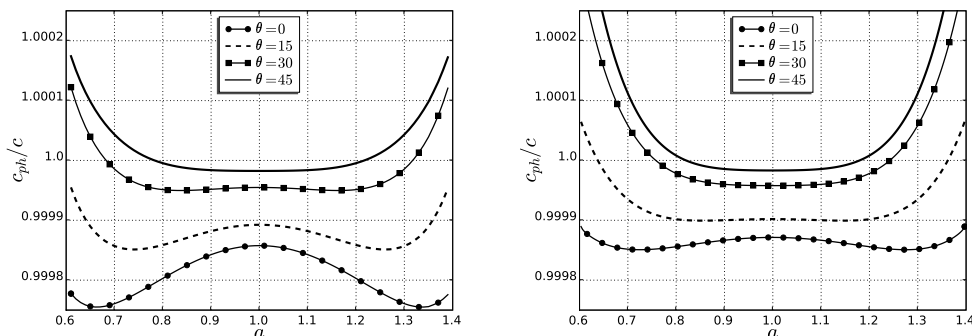


Figure 5: Normalized phase velocity estimates of the cubic Legendre SEM computed with the eigenvalue that is closer to the acoustic mode (left, see also [7, Fig. 12.8]) and the Rayleigh quotient (right). We consider nine grid points per wavelength. For comparison purposes, we use the parameter a from [7, Fig. 12.8] that locates the central node of the patch (i.e., the central node coordinates of the patch $[0, h] \times [0, h]$ are $(ah, (3a - 1)h/2)$, $0.6 \leq a \leq 1.4$).

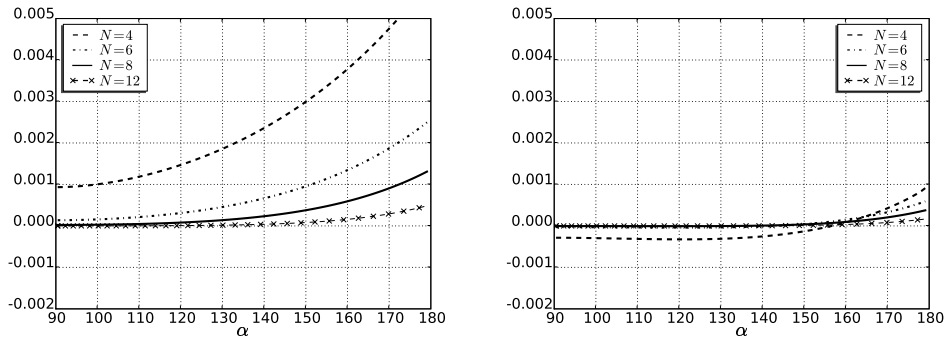


Figure 6: Average phase velocity error of GLC (left) and GLL (right) methods versus element distortion for the patch (a) with a grid resolution of four grid points per wavelength.

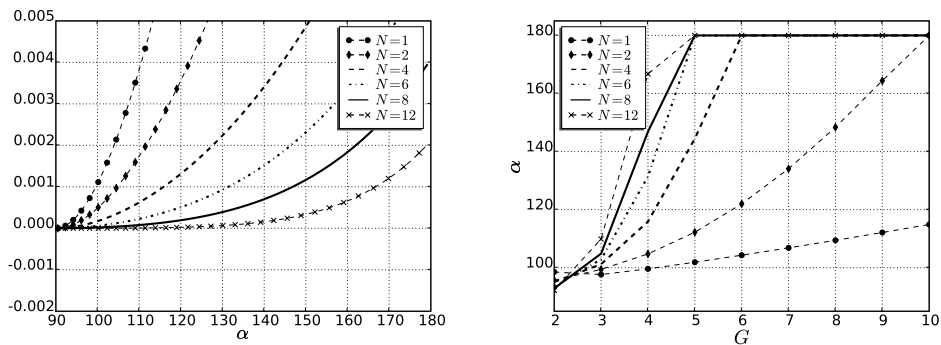


Figure 7: Study of maximum phase velocity deviation of the GLC method with respect to the undistorted mesh in the patch (a). Left: maximum deviation when the number of grid points per wavelength is $G = 4$; right: maximum distortion parameter such that the maximum deviation is 0.1%.

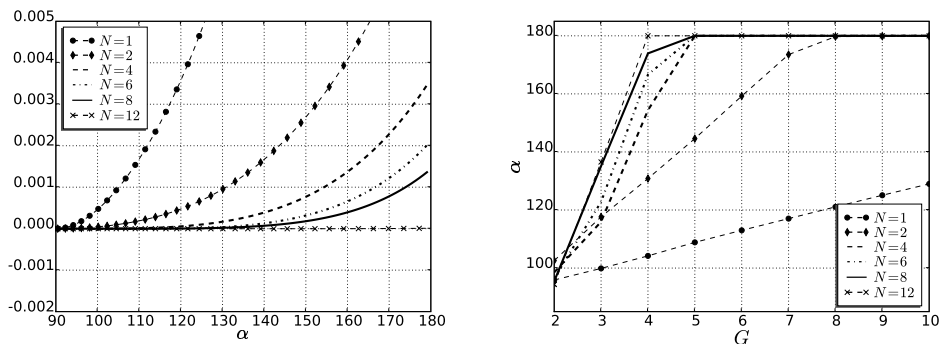


Figure 8: Same as Fig. 7, except with the GLL method.

$\kappa = \kappa(\cos\theta, \sin\theta)$, $\theta = 0, \pi/24, 2\pi/24, \dots, 2\pi$. We see that the error grows with the element distortion and decreases as the element order increases. Moreover, higher order elements are less sensitive to element distortion.

In Figs. 7-8 we consider a slightly different quantity: the relative deviation of the numerical phase velocity on a deformed mesh ($\alpha > 90^\circ$) with respect to the numerical

phase velocity when $\alpha = 90^\circ$; that is, given $c^*(\alpha) = \omega^* / \kappa$, we consider

$$\Delta c^*(\alpha) = \frac{c^*(\alpha) - c^*(90^\circ)}{c^*(90^\circ)}. \tag{4.2}$$

Besides the variation of phase deviation with respect to α , we also indicate the maximum element distortion, such that the phase deviation is below 0.1% as a function of the number of grid points per wavelength. We also contrast the spectral element methods with low-order finite element methods. As expected, the increase of the number of grid points per wavelength G makes the error less sensitive to the element distortion. On the other hand, low order elements are very sensitive to the distortion.

Figs. 9-10 illustrate the numerical anisotropy of each SEM when $G = 4$. We first set the polynomial degree as $N = 6$ and take $\alpha = 90^\circ, 110^\circ, 130^\circ$. Then, we fix $\alpha = 130^\circ$ and let $N = 4, 6, 8, 12$. For viewing purposes, we emphasize the error by displaying the scaled

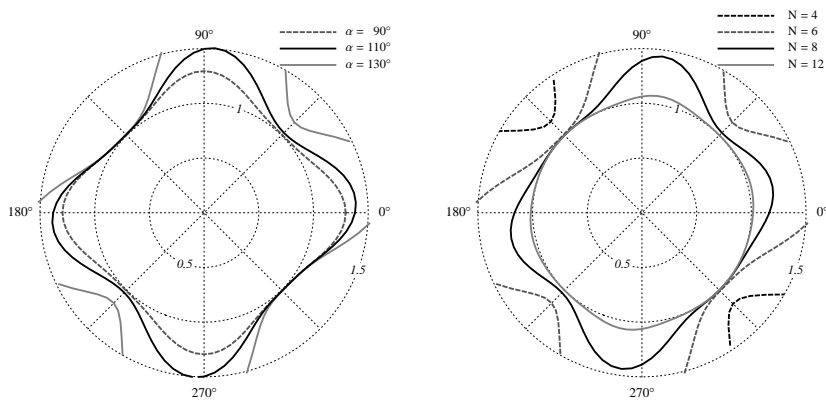


Figure 9: Polar graph of phase velocity error of the GLC method in the patch (a) with a grid resolution of four grid points per wavelength and $N = 6$ (left) and $N = 4, \dots, 12$ with $\alpha = 130^\circ$ (right). The error is scaled as $1 + 10^3 \epsilon$.

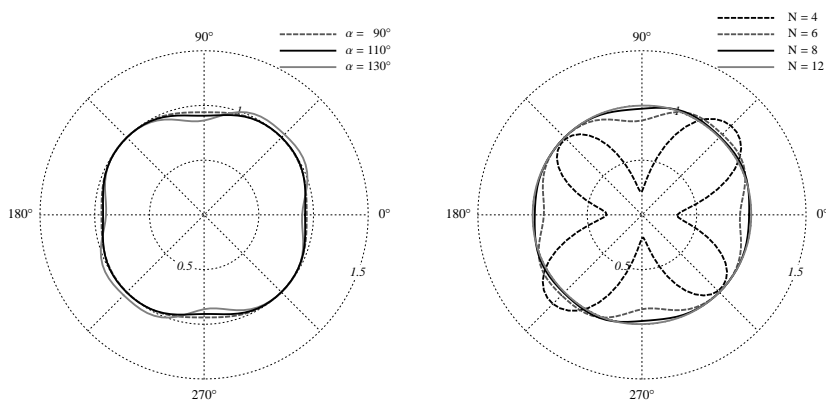


Figure 10: Same as Fig. 9, except with the GLL method.

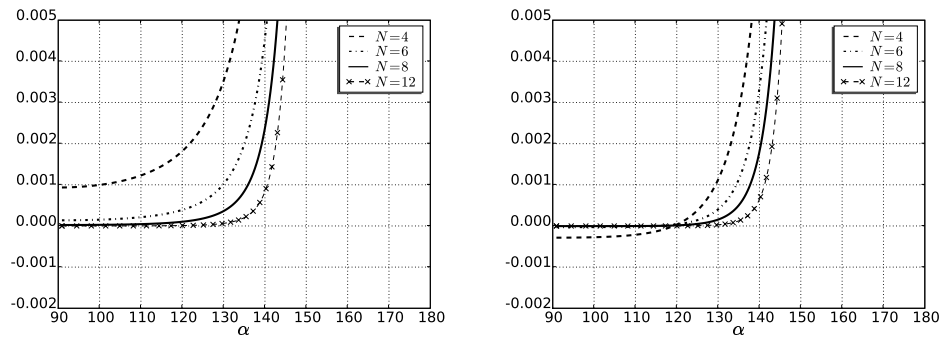


Figure 11: Average phase velocity error of GLC (left) and GLL (right) methods versus element distortion for the patch (b) with a grid resolution of four grid points per wavelength.

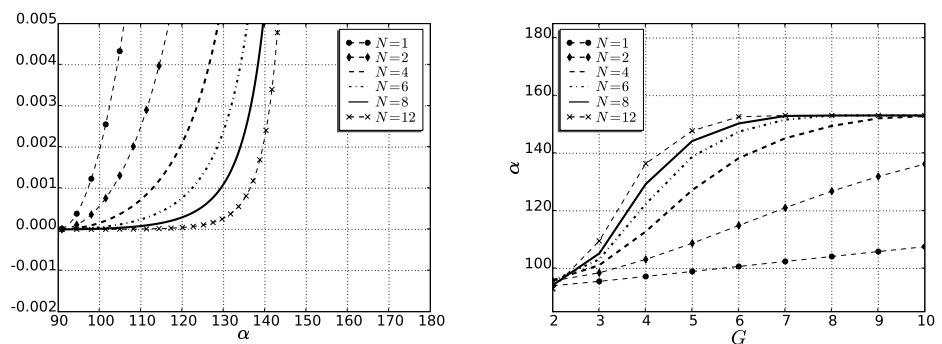


Figure 12: Study of maximum phase velocity deviation of the GLC method with respect to the undistorted mesh in the patch (b). Left: maximum deviation when the number of grid points per wavelength is $G = 4$; right: maximum distortion parameter such that the maximum deviation is 0.1%.

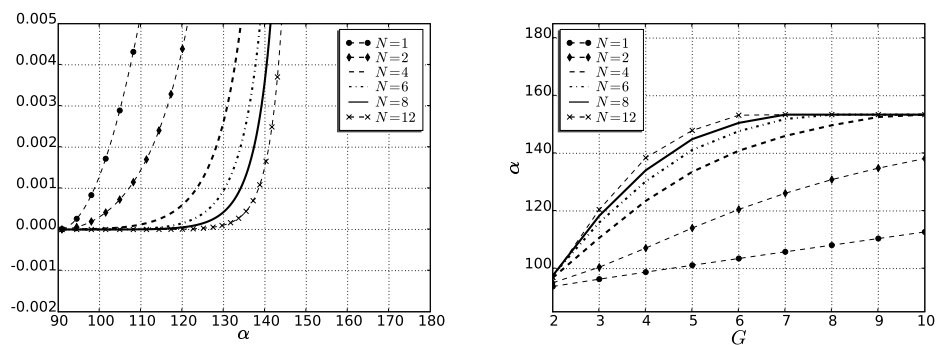


Figure 13: Same as Fig. 12, except with the GLL method.

phase error $1 + 10^3 \varepsilon$. We can see that the numerical anisotropy of the error depends on the distortion and decreases as the element order increases.

The numerical experiments are repeated for all the other patches and the results show a similar behavior. The same comments as above apply and will be not repeated in the following.

The patch (b) considers the situation where quadrilateral elements collapse into triangles. Fig. 11 shows average phase velocity errors, as in Fig. 6. Notice that in this case the maximum distortion angle, for geometrical reasons, is smaller than in the other cases and that the error blows up as the distortion angle approaches $\cos^{-1}(-2/\sqrt{5})$. In the distortion limit, when all quadrilaterals collapse into triangles, the angle is actually $\cos^{-1}(2/\sqrt{5})$.

Analogously, Figs. 12-13 consider the maximum phase deviation, as in Figs. 7-8, while Figs. 14-15 present the numerical anisotropy of the methods GLC and GLL in the patch (b). Note from Fig. 12 (right) and Fig. 13 (right) that the we need a larger number of grid points per wavelength (with respect to other patches) to reduce the sensitivity of the error with the element distortion.

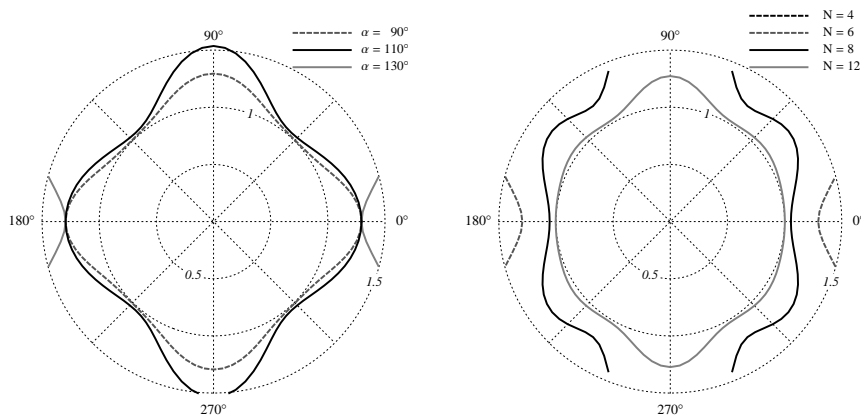


Figure 14: Polar graph of phase velocity error of the GLC method in the patch (b) with a grid resolution of four grid points per wavelength and $N=6$ (left) and $N=4, \dots, 12$ with $\alpha=130^\circ$ (right). The error is scaled as $1+10^3\varepsilon$.

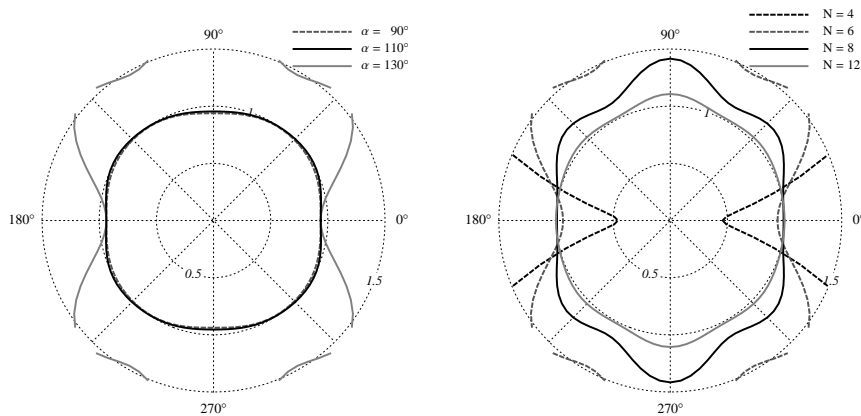


Figure 15: Same as Fig. 14, except with the GLL method.

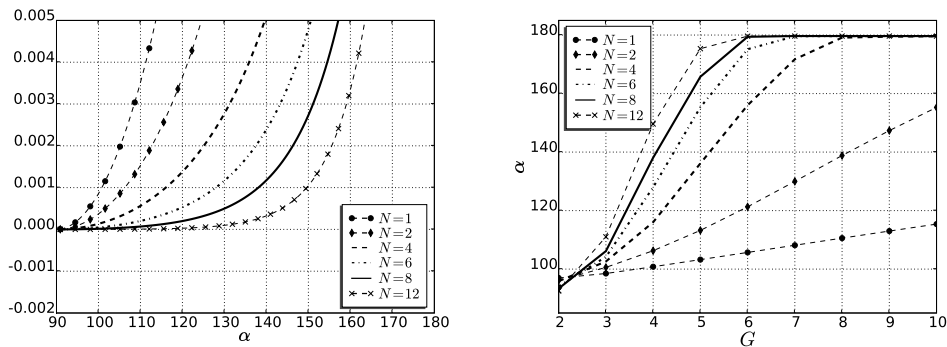


Figure 16: Study of maximum phase velocity deviation of the GLC method with respect to the undistorted mesh in the patch (c). Left: maximum deviation when the number of grid points per wavelength is $G=4$; right: maximum distortion parameter such that the maximum deviation is 0.1%.

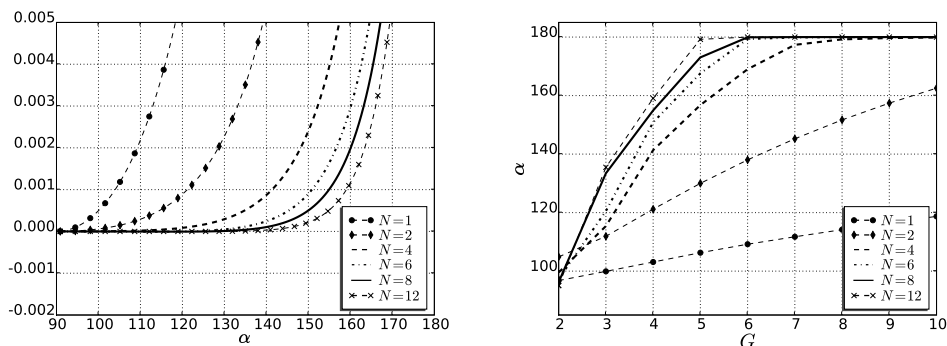


Figure 17: Same as Fig. 16, except with the GLL method.

In patch (c) we have the presence of a sliver element. Although the distortion seems more severe than in the former examples, we found that the phase deviations (Figs. 16-17) are very similar to those observed on patch (b). This can be explained since we keep the number of grid points per wavelength constant with respect to the distortion parameter α . The area of the upper right element on patch (c) becomes small as α increases, but the concentration of grid points within this element increases with α , compensating the distortion effect.

Patch (d) also suffers from slivering. Moreover, the diameter of the central element approaches the diameter of the entire patch, hence this element remains under-sampled (with respect to the other elements) along one direction. In order to have errors and deviations with the same order of magnitude as in the other examples, we use six grid points per wavelength in this patch. Note from Figs. 18-20 that the difference between low-order and high-order elements is more evident on patch (d). This indicates the importance of using higher-order spectral elements when sliver elements are present.

Remark 4.1. The spectral element method with GLC collocation points generates larger dispersion errors, which overestimate the correct phase velocity. Such a behavior is usu-

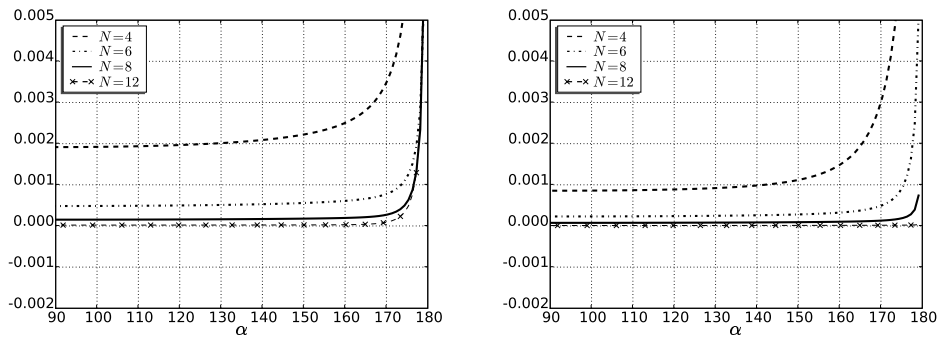


Figure 18: Average phase velocity error of GLC (left) and GLL (right) methods versus element distortion for the patch (d) with six grid points per wavelength.

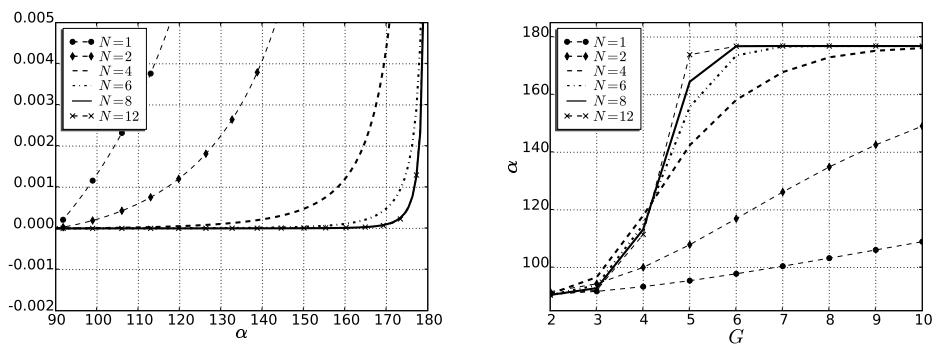


Figure 19: Study of maximum phase velocity deviation of the GLC method with respect to the undistorted mesh in the patch (d). Left: maximum deviation when the number of grid points per wavelength is $G = 6$; right: maximum distortion parameter such that the maximum deviation is 0.1%.

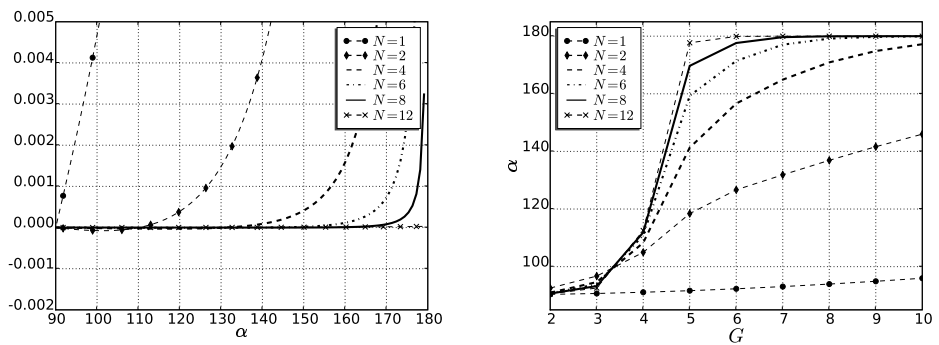


Figure 20: Same as Fig. 19, except with the GLL method.

ally present in consistent formulations of the mass matrix and may be corrected by combining consistent and lumped formulations [6] or by employing reduced integration, as the GLL method [8]. This is illustrated in Fig. 21, where the M-optimal blended spectral element method, a weighted consistent and lumped formulation with GLC points [32] is compared with the GLL method.

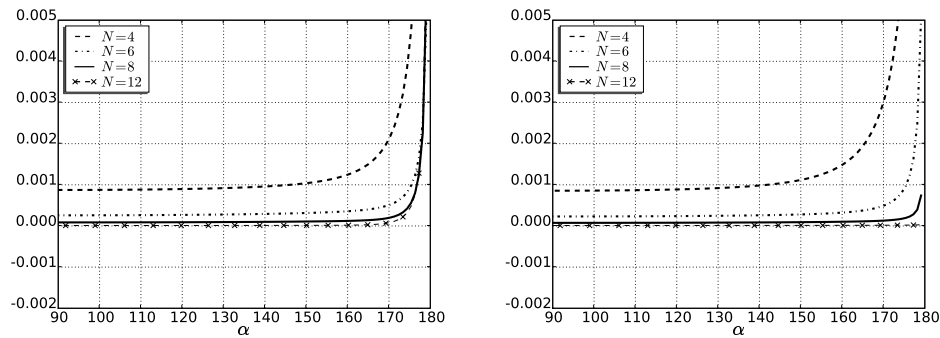


Figure 21: Average phase velocity error of M-OB (left) and GLL (right) methods versus element distortion for the patch (d) with six grid points per wavelength.

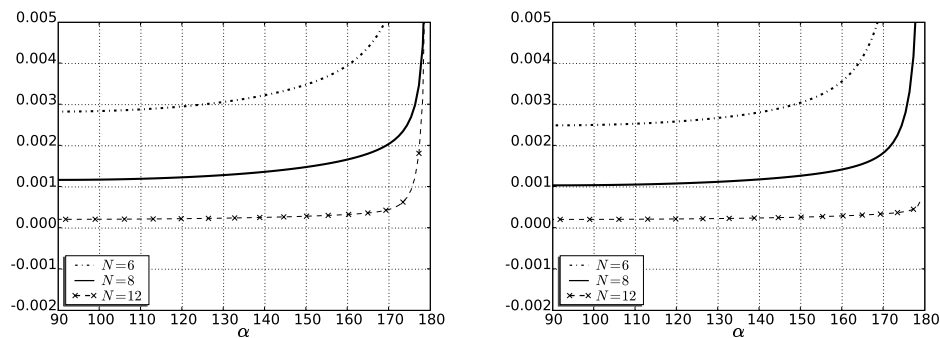


Figure 22: Average group velocity error of M-OB (left) and GLL (right) methods versus element distortion for the patch (d) with six grid points per wavelength. The error of fourth-degree elements, which is above 0.005 on both methods, is not shown in this figure.

Remark 4.2. For simplicity, the results presented herein were based on the error on phase velocity. By taking derivatives with respect to κ on both sides of (2.4), we can retrieve formulae for the numerical group velocity and carry out the analysis using this quantity. For instance, Fig. 22 is the counterpart of Fig. 21 when group velocity is considered. Note that the errors of the spectral elements of degree $N=8,12$ are low also in this case. To the authors' knowledge, up to date there is no analytical or numerical study of group velocity error of high-order finite element methods on distorted meshes.

5 Conclusions

We have studied the numerical dispersion of two differing two-dimensional spectral element methods using meshes generated by repetition of distorted elements. In practical applications a finite element mesh may present several patterns of distortion. We consider each pattern individually, extending the approach reported in [7] for more complex cases, and for each we obtain the maximum element distortion allowed for both a fixed error tolerance and an element degree N . In the case of real simulations, the average error

will be therefore in the tolerance range if all elements in the mesh have a distortion less than the allowed maximum.

We found that the dispersion errors of Gauss-Lobatto-Legendre (GLL) spectral element methods remain insensitive to mesh distortion until near the distortion limit in the examples above. This provides additional support for the claim that GLL spectral element methods perform well with the standard set of integration points even for large distortions [7, 20]. We note that there is not a consensus regarding the need for overintegration of GLL spectral element methods [22].

We enhanced spectral element methods based on Gauss-Lobatto-Chebyshev (GLC) points by using a double-grid calculation of the inverse Jacobian function. This technique increases the robustness of GLC methods and at the same time preserves the implementation framework of spectral elements, and may be useful in other applications such as fluid mechanics and elasticity.

In general, we can see that the numerical dispersion of low order finite elements ($N=1,2$) is significantly larger than expected from studies on rectangular meshes [7, 21, 24] when distortion takes place, but spectral elements with degree $N \geq 6$ are very robust and perform well even at large distortion and in the presence of slivering.

Appendix: Element calculations

For the sake of completeness and in order to introduce some notation used in this work, on this appendix we review some classic finite element calculations involving isoparametric transformations [17]. We also provide the details of our proposed double-grid representation of the inverse Jacobian.

Let us evaluate the products $\overline{w}^e T M^e w^e$ and $\overline{w}^e T K^e w^e$ from (2.10) in an arbitrary element Ω^e . It is convenient to represent node coordinates and nodal values of functions as $(N+1) \times (N+1)$ arrays, which we indicate with brackets. For instance,

$$[X^e] = \begin{bmatrix} X_{0,0}^e & X_{0,1}^e & \cdots & \cdots & X_{0,N}^e \\ X_{1,0}^e & X_{1,1}^e & \cdots & \cdots & X_{1,N}^e \\ \vdots & \cdots & \cdots & \cdots & \cdots \\ X_{N,0}^e & X_{N,1}^e & \cdots & \cdots & X_{N,N}^e \end{bmatrix} \quad (\text{A.1})$$

is the matrix representation of the x -coordinates of the element nodes of Ω^e (similarly for $[Y^e]$), while we also represent the vector w^e by the matrix $[w^e]$.

The element integrals in the reference element $\hat{\Omega} = [-1,1] \times [-1,1]$ are mapped to Ω^e by the isoparametric transformation

$$\begin{cases} X(\xi, \eta) = \sum_{q_1, q_2=0}^N X_{q_1, q_2}^e \phi_{q_1}(\xi) \phi_{q_2}(\eta), \\ Y(\xi, \eta) = \sum_{q_1, q_2=0}^N Y_{q_1, q_2}^e \phi_{q_1}(\xi) \phi_{q_2}(\eta), \end{cases} \quad (\text{A.2})$$

where $\phi_p(\zeta)$, with $\zeta \in [-1,1]$, is the p -th 1D Lagrange interpolation shape function of degree N defined by $\phi_p(\zeta_q) = \delta_{p,q}$, $0 \leq p, q \leq N$. Here ζ_q represents the q -th collocation point in $[-1,1]$ and $(\zeta, \eta) \in \hat{\Omega}$. Analogously, we define

$$w(\zeta, \eta) = \sum_{q_1, q_2=0}^N w_{q_1, q_2}^e \phi_{q_1}(\zeta) \phi_{q_2}(\eta). \tag{A.3}$$

We have from (A.2) that

$$\overline{w}^T \mathbf{M}^e w^e = \int_{-1}^1 \int_{-1}^1 \overline{w(\zeta, \eta)} w(\zeta, \eta) J(\zeta, \eta) d\zeta d\eta, \tag{A.4}$$

$$\overline{w}^T \mathbf{K}^e w^e = \int_{-1}^1 \int_{-1}^1 \overline{\hat{\nabla} w(\zeta, \eta)} \cdot \hat{\nabla} w(\zeta, \eta) \frac{1}{J(\zeta, \eta)} d\zeta d\eta, \tag{A.5}$$

where $J(\zeta, \eta) = \partial_{\zeta} X(\zeta, \eta) \partial_{\eta} Y(\zeta, \eta) - \partial_{\zeta} Y(\zeta, \eta) \partial_{\eta} X(\zeta, \eta)$ is the determinant of the Jacobian of the transformation (A.2) and

$$\hat{\nabla} w(\zeta, \eta) = \begin{bmatrix} \hat{\nabla}_1 w(\zeta, \eta) \\ \hat{\nabla}_2 w(\zeta, \eta) \end{bmatrix} = \begin{bmatrix} \partial_{\eta} Y(\zeta, \eta) \partial_{\zeta} w(\zeta, \eta) - \partial_{\zeta} Y(\zeta, \eta) \partial_{\eta} w(\zeta, \eta) \\ -\partial_{\eta} X(\zeta, \eta) \partial_{\zeta} w(\zeta, \eta) + \partial_{\zeta} X(\zeta, \eta) \partial_{\eta} w(\zeta, \eta) \end{bmatrix}. \tag{A.6}$$

The nodes of the element Ω^e are related to the spectral element collocation points by the isoparametric transformation (A.2). These points are defined by the tensor product of the 1D collocation points ζ_p ($0 \leq p \leq N$). In the following we characterize the arrays that sample J and $\hat{\nabla} w$ at the collocation points.

The derivative matrix D is defined as

$$D_{p,q} = \partial_{\zeta} \phi_q(\zeta_p) \equiv \left. \frac{\partial \phi_q(\zeta)}{\partial \zeta} \right|_{\zeta=\zeta_p}. \tag{A.7}$$

Let $[g]$ be a $(N+1) \times (N+1)$ array. The polynomial $g(\zeta, \eta)$ that interpolates $[g]$ at the local grid nodes $(\zeta_{q_1}, \zeta_{q_2})$, $0 \leq q_1, q_2 \leq N$, is defined as

$$g(\zeta, \eta) = \sum_{q_1, q_2=0}^N g_{q_1, q_2} \phi_{q_1}(\zeta) \phi_{q_2}(\eta). \tag{A.8}$$

Let us define $[\partial_{\zeta} g]$ as

$$\partial_{\zeta} g_{p_1, p_2} = \partial_{\zeta} g(\zeta_{q_1}, \zeta_{q_2}), \quad 0 \leq p_1, p_2 \leq N,$$

we have that

$$\partial_{\zeta} g_{p_1, p_2} = \sum_{q_1, q_2=0}^N g_{q_1, q_2} (\partial_{\zeta} \phi_{q_1}(\zeta_{p_1})) \phi_{q_2}(\eta_{p_2}) = \sum_{q_1=0}^N D_{p_1, q_1} g_{q_1, p_2}. \tag{A.9}$$

In the same fashion,

$$\partial_\eta g_{p_1,p_2} = \partial_\eta g(\zeta_{q_1}, \zeta_{q_2}) = \sum_{q_2=0}^N D_{p_2,q_2} g_{p_1,q_2}; \tag{A.10}$$

that is,

$$[\partial_\zeta g] = \mathbf{D}[g] \quad \text{and} \quad [\partial_\eta g] = [g]\mathbf{D}^T.$$

Thus, we can write the nodal values of J , $\hat{\nabla}_1 w$ and $\hat{\nabla}_2 w$ in matrix form (see also [17]) as

$$[J] = (\mathbf{D}[X^e]) \circ ([Y^e]\mathbf{D}^T) - (\mathbf{D}[Y^e]) \circ ([X^e]\mathbf{D}^T), \tag{A.11}$$

$$[\nabla_1 w] = ([Y^e]\mathbf{D}^T) \circ (\mathbf{D}[w^e]) - (\mathbf{D}[Y^e]) \circ ([w^e]\mathbf{D}^T), \tag{A.12}$$

$$[\nabla_2 w] = (\mathbf{D}[X^e]) \circ ([w^e]\mathbf{D}^T) - ([X^e]\mathbf{D}^T) \circ (\mathbf{D}[w^e]), \tag{A.13}$$

where \circ denotes the Haddamard (termwise) product [19]:

$$\mathbf{C} = \mathbf{A} \circ \mathbf{B} \implies C_{p,q} = A_{p,q} B_{p,q}. \tag{A.14}$$

When Gauss-Lobatto-Legendre (GLL) collocation points are employed to define the shape functions ϕ_p (i.e., ζ_0, \dots, ζ_N are roots of $(1-\zeta^2)\partial_\zeta P_N(\zeta)$, where P_N denotes the Legendre polynomial of degree N), the standard practice is to use these points also as quadrature points. In this case, the quadrature is exact for polynomials of degree $2N-1$ in each spatial direction [3]. If $[W]$ is the array that contains the integration weights corresponding to $(\zeta_{q_1}, \zeta_{q_2})$ and $(1/[J])_{q_1,q_2} = 1/J_{q_1,q_2}$, $0 \leq q_1, q_2 \leq N$, then

$$\overline{w}^T \mathbf{M}^e w^e = [W]: \left(\overline{[w^e]} \circ [w^e] \circ [J] \right), \tag{A.15}$$

$$\overline{w}^T \mathbf{K}^e w^e = [W]: \left(\overline{[\nabla_1 w]} \circ [\nabla_1 w] \circ \frac{1}{[J]} + \overline{[\nabla_2 w]} \circ [\nabla_2 w] \circ \frac{1}{[J]} \right), \tag{A.16}$$

where the colon sign denotes the double-contraction operator:

$$\mathbf{A}:\mathbf{B} = \sum_{p,q=0}^N A_{p,q} B_{p,q}. \tag{A.17}$$

Korczak and Patera [17] introduced an integration procedure that does not use integration points and weights in the case of Gauss-Lobatto-Chebyshev (GLC) points $\zeta_p = -\cos(\pi p/N)$, $0 \leq p \leq N$. Let \mathbf{B} be defined as

$$B_{l,p,q} = \int_{-1}^1 \phi_l(\zeta) \phi_p(\zeta) \phi_q(\zeta) d\zeta = \sum_{i=0}^N \sum_{j=0}^N \sum_{k=0}^N s_{l,i} s_{p,j} s_{q,k} \mathbf{C}_{i,j,k}, \tag{A.18}$$

with

$$\mathbf{C}_{l,p,q} = \int_{-1}^1 T_l(\zeta) T_p(\zeta) T_q(\zeta) d\zeta, \tag{A.19}$$

where $T_p(\zeta) = \cos(p \cos^{-1}(\zeta))$ is the p -th Chebyshev polynomial, and

$$s_{p,q} = \frac{2}{Nc_p c_q} \cos\left(q \frac{\pi(N-p)}{N}\right), \quad c_p = \begin{cases} 1, & 0 < p < N, \\ 2, & p = 0, N. \end{cases} \quad (\text{A.20})$$

Let us expand $w(\zeta, \eta)$ and $J(\zeta, \eta)$ with respect to the Lagrange polynomials ϕ_p as in (A.3) and substitute these expansions into (A.4):

$$\begin{aligned} & \overline{w}^e{}^T \mathbf{M}^e w^e \\ &= \int_{-1}^1 \int_{-1}^1 \sum_{p_1, p_2=0}^N \overline{w}_{p_1, p_2}^e \phi_{p_1}(\zeta) \phi_{p_2}(\eta) \sum_{q_1, q_2=0}^N w_{q_1, q_2}^e \phi_{q_1}(\zeta) \phi_{q_2}(\eta) \sum_{l_1, l_2=0}^N J_{l_1, l_2} \phi_{l_1}(\zeta) \phi_{l_2}(\eta) d\zeta d\eta \\ &= \sum_{p_1, \dots, l_2=0}^N \overline{w}_{p_1, p_2}^e w_{q_1, q_2}^e J_{l_1, l_2} \int_{-1}^1 \phi_{l_1}(\zeta) \phi_{p_1}(\zeta) \phi_{q_1}(\zeta) d\zeta \int_{-1}^1 \phi_{l_2}(\eta) \phi_{p_2}(\eta) \phi_{q_2}(\eta) d\eta \\ &= \sum_{p_1, p_2=0}^N \sum_{q_1, q_2=0}^N \overline{w}_{p_1, p_2}^e w_{q_1, q_2}^e \sum_{l_1, l_2=0}^N J_{l_1, l_2} B_{l_1, p_1, q_1} B_{l_2, p_2, q_2}, \end{aligned} \quad (\text{A.21})$$

or in tensor notation,

$$\overline{w}^e{}^T \mathbf{M}^e w^e = \text{tr}(\overline{[w^e]}^T \cdot \mathbf{B}^+ \cdot [w^e]), \quad \mathbf{B}^+ = \mathbf{B}^T \cdot [\mathbf{J}] \cdot \mathbf{B}. \quad (\text{A.22})$$

We remark that the single contraction and the transposition operators above are taken in the generalized sense [30], for instance:

$$(\mathbf{B}^T)_{l,p,q} = B_{p,q,l} \quad \text{and} \quad ([\mathbf{J}] \cdot \mathbf{B})_{l,p,q} = \sum_{j=0}^N J_{l,j} B_{j,p,q}. \quad (\text{A.23})$$

Moreover, denoting with $\text{tr}(\cdot)$ also the double contraction of a fourth-rank tensor:

$$\text{tr}(\mathbf{A}) = \sum_{p,q=0}^N A_{p,q,p,q}, \quad (\text{A.24})$$

we have, analogously, that

$$\overline{w}^e{}^T \mathbf{K}^e w^e = \text{tr}(\overline{[\nabla_1 w]}^T \cdot \mathbf{B}^- \cdot [\nabla_1 w] + \overline{[\nabla_2 w]}^T \cdot \mathbf{B}^- \cdot [\nabla_2 w]), \quad (\text{A.25})$$

where $\mathbf{B}^- = \mathbf{B}^T \cdot (1/[\mathbf{J}]) \cdot \mathbf{B}$. Note that the presence of the rational function $1/[\mathbf{J}]$ in the integrand renders Eq. (A.25) inexact. As shown in the numerical tests, such an inaccuracy does not pose problems if the polynomial degree of the shape functions is large enough, but it does lead to dispersion errors on some spectral elements of interest, such as fourth-degree polynomials [5].

In order to avoid dispersion errors on spectral elements of lower degree, we propose a simple approach based on the double-grid spectral element method [31]. We represent the inverse Jacobian with polynomials with an independent set of shape functions of higher degree, i.e.,

$$\frac{1}{J}(\xi, \eta) = \sum_{q_1, q_2=0}^L \frac{1}{[[J]]_{q_1, q_2}} \phi_{q_1}^L(\xi) \phi_{q_2}^L(\eta), \quad (\text{A.26})$$

where $\phi_p^L(\xi)$ is the p -th 1D Lagrange interpolation shape function of degree $L, L \geq N$, while $[[J]]$ is the $(L+1) \times (L+1)$ matrix that samples $J(\xi, \eta)$ at the collocation points of the temporary grid defined by $(\xi_{q_1}^L, \eta_{q_2}^L), 0 \leq q_1, q_2 \leq L$. We use the notation $[[\cdot]]$ for $(L+1) \times (L+1)$ matrices to avoid ambiguity with the notation $[\cdot]$ for $(N+1) \times (N+1)$ matrices.

Substituting (A.26) and (A.3) into (A.5), we find

$$\overline{w}^e T \mathbf{K}^e w^e = \text{tr}(\overline{[\nabla_1 w]}^T \cdot \mathbf{B}^- \cdot [\nabla_1 w] + \overline{[\nabla_2 w]}^T \cdot \mathbf{B}^- \cdot [\nabla_2 w]), \quad (\text{A.27})$$

$$\mathbf{B}^- = \mathbf{B}^T \cdot \left(\frac{1}{[[J]]} \right) \cdot \mathbf{B}, \quad \mathcal{B}_{l,p,q} = \sum_{i=0}^L \sum_{j=0}^N \sum_{k=0}^N s_{l,i}^L s_{p,q} s_{q,k} \mathcal{C}_{i,j,l}, \quad (\text{A.28})$$

where $\mathcal{C}_{l,p,q}$ and $s_{p,q}$ are defined in (A.19)-(A.20), whereas

$$s_{p,q}^L = \frac{2}{L C_p^L C_q^L} \cos\left(q \frac{\pi(L-p)}{L}\right), \quad c_p^L = \begin{cases} 1, & 0 < p < L, \\ 2, & p = 0, L. \end{cases} \quad (\text{A.29})$$

Acknowledgments

We gratefully acknowledge the anonymous reviewers whose constructive comments contributed to improve the manuscript. This work was funded in part by the SPICE-Marie Curie RTN project (contract MRTN-CT-2003-504267). Saulo P. Oliveira was also partially supported by the ICTP Programme for Training and Research in Italian Laboratories, Trieste, Italy, and by CNPq, Brazil, under grant 314553/2009-6.

References

- [1] N. Abboud and P. Pinsky, Finite element dispersion analysis for the three-dimensional second-order scalar wave equation, *Int. J. Numer. Meth. Eng.*, 35(6) (1992), 1183–1218.
- [2] D. Burnett, *Finite Element Analysis: From Concepts to Applications*, Addison-Wesley, 1987.
- [3] C. Canuto, M. Hussaini, A. Quarteroni, and T. Zang, *Spectral Methods in Fluid Dynamics*, Springer-Verlag, New York, NY, 1987.
- [4] E. Chaljub, Y. Capdeville, and J. P. Vilotte, Solving elastodynamics in a fluid-solid heterogeneous sphere: a parallel spectral element approximation on non-conforming grids, *J. Comput. Phys.*, 187(2) (2003), 457–491.
- [5] E. Chaljub, D. Komatitsch, J.-P. Vilotte, Y. Capdeville, B. Valette, and G. Festa, Spectral element analysis in seismology, in Ru-Shan Wu and Valérie Maupin, editors, *Advances in*

- Wave Propagation in Heterogeneous Media, volume 48 of Advances in Geophysics, pages 365–419, Elsevier, 2007.
- [6] M. Christon, The influence of the mass matrix on the dispersive nature of the semi-discrete, second-order wave equation, *Comput. Methods. Appl. Mech. Engrg.*, 173(1–2) (1999), 147–166.
 - [7] G. Cohen, *Higher-Order Numerical Methods for Transient Wave Equations*, Springer-Verlag, New York, NY, 2002.
 - [8] G. Cohen, P. Joly, and N. Tordjman, Higher-order finite elements with mass-lumping for the 1D wave equation, *Finite. Elem. Anal. Des.*, 16(3–4) (1994), 329–336.
 - [9] W. Dauksher and A. Emery, The solution of elastostatic and elastodynamic problems with Chebyshev spectral finite elements, *Comput. Methods. Appl. Mech. Engrg.*, 188(1-3) (2000), 217–233.
 - [10] J. De Basabe and M. Sen, Grid dispersion and stability criteria of some common finite-element methods for acoustic and elastic wave equations, *Geophysics.*, 72(6) (2007), T81–T95.
 - [11] J. De Basabe and M. Sen, Comment on “dispersion analysis of spectral element methods for elastic wave propagation”, *Wave. Motion.*, 46(1) (2009), 92–93.
 - [12] M. O. Deville, P. Fischer, and E. Mund, *High-Order Methods for Incompressible Fluid Flow*, Cambridge University Press, 2002.
 - [13] J. S. Hesthaven and T. Warburton, Nodal high-order methods on unstructured grids, I: time-domain solution of Maxwell’s equations, *J. Comput. Phys.*, 181(1) (2002), 186–221.
 - [14] M. E. Hochstenbach and H. A. van der Vorst, Alternatives to the Rayleigh quotient for the quadratic eigenvalue problem, *SIAM J. Sci. Comput.*, 25(2) (2003), 591–603.
 - [15] T. Hughes, *The Finite Element Method*, Prentice-Hall, Englewood Cliffs, NJ, 1987.
 - [16] D. Komatitsch and J. P. Vilotte, The spectral-element method: an efficient tool to simulate the seismic response of 2D and 3D geological structures, *Bull. Seismol. Soc. Am.*, 88(2) (1998), 368–392.
 - [17] K. Korczak and A. Patera, An isoparametric spectral element method for solution of the Navier-Stokes equations in complex geometry, *J. Comput. Phys.*, 62(2) (1986), 361–382.
 - [18] G. Laurenzano, E. Priolo, and E. Tondi, 2D numerical simulations of earthquake ground motion: examples from the Marche Region, Italy, *J. Seismol.*, 12(3) (2008), 395–412.
 - [19] H. Lütkepohl, *Handbook of Matrices*, John Wiley & Sons, Chichester, UK, 1996.
 - [20] Y. Maday and E. Rønquist, Optimal error analysis of spectral methods with emphasis on non-constant coefficients and deformed geometries, *Comput. Methods. Appl. Mech. Eng.*, 80(1–3) (1990), 91–115.
 - [21] K. Marfurt, Appendix-analysis of higher order finite-element methods, in K. Kelly and K. Marfurt, editors, *Numerical modeling of seismic wave propagation*, number 13, in *Geophysics Reprint Series*, pages 516–520, Soc. Expl. Geophys., Tulsa, OK, 1990.
 - [22] J. M. Melenk, K. Gerdes, and C. Schwab, Fully discrete *hp*-finite elements: fast quadrature, *Comput. Methods. Appl. Mech. Engrg.*, 190(32-33) (2001), 4339–4364.
 - [23] E. D. Mercerat, J. P. Vilotte, and F. J. Sanchez-Sesma, Triangular spectral element simulation of two-dimensional elastic wave propagation using unstructured triangular grids, *Geophys. J. Int.*, 166(2) (2006), 679–690.
 - [24] W. Mulder, Spurious modes in finite-element discretizations of the wave equation may not be all that bad, *Appl. Numer. Math.*, 30(4) (1999), 425–445.
 - [25] S. P. Oliveira and G. Seriani, DFT modal analysis of spectral element methods for the 2D elastic wave equation, *J. Comput. Appl. Math.*, 234 (2010), 1717–1724.

- [26] A. Patera, A spectral element method for fluid dynamics: Laminar flow in a channel expansion, *J. Comput. Phys.*, 54(3) (1984), 468–488.
- [27] E. Priolo, 2-D spectral element simulations of destructive ground shaking in Catania (Italy), *J. Seismol.*, 3(3) (1999), 289–309.
- [28] E. Priolo, J. Carcione, and G. Seriani, Numerical simulation of interface waves by high-order spectral modeling techniques, *J. Acoust. Soc. Am.*, 95(2) (1994), 681–693.
- [29] M. Proot and M. Gerritsma, Application of the least-squares spectral element method using Chebyshev polynomials to solve the incompressible Navier-Stokes equations, *Numer. Algorithms.*, 38(1-3) (2005), 155–172.
- [30] G. Seriani, 3-D large-scale wave propagation by spectral element method on Cray T3E multiprocessor, *Comput. Methods. Appl. Mech. Engrg.*, 164(1-2) (1998), 235–247.
- [31] G. Seriani, Double-grid Chebyshev spectral elements for acoustic wave modeling, *Wave. Motion.*, 39(4) (2004), 351–360.
- [32] G. Seriani and S. P. Oliveira, Optimal blended spectral element operators for forward modeling, *Geophys.*, 72(5) (2007), SM95–SM106.
- [33] G. Seriani and S. P. Oliveira, Dispersion analysis of spectral element methods for acoustic wave propagation, *J. Comput. Acoust.*, 16(4) (2008), 531–561.
- [34] G. Seriani and S. P. Oliveira, Dispersion analysis of spectral element methods for elastic wave propagation, *Wave. Motion.*, 45(6) (2008), 729–744.
- [35] G. Seriani and S. P. Oliveira, Reply to comment on “dispersion analysis of spectral element methods for elastic wave propagation”, *Wave. Motion.*, 46(1) (2009), 94–95.
- [36] G. Seriani and E. Priolo, Spectral element method for acoustic wave simulation in heterogeneous media, *Finite. Elem. Anal. Des.*, 16(3-4) (1994), 337–348.
- [37] D. Stanescu, D. Ait-Ali-Yahia, W. G. Habashi, and M. P. Robichaud, Spectral element method for linear fan tone noise radiation, *AIAA J.*, 42(4) (2004), 696–705.
- [38] D. White, Numerical dispersion of a vector finite element method on skewed hexahedral grids, *Commun. Numer. Methods. Eng.*, 16(1) (2000), 47–55.
- [39] A. Zak, A novel formulation of a spectral plate element for wave propagation in isotropic structures, *Finite. Elem. Anal. Des.*, 45(10) (2009), 650–658.
- [40] S. Zhang, Numerical integration with Taylor truncations for the quadrilateral and hexahedral finite elements, *J. Comput. Appl. Math.*, 205(1) (2007), 325–342.